Volume 12
Number 18
14 May 2024
Pages 4281–4524

Journal of Materials Chemistry B

Materials for biology and medicine

rsc.li/materials-b

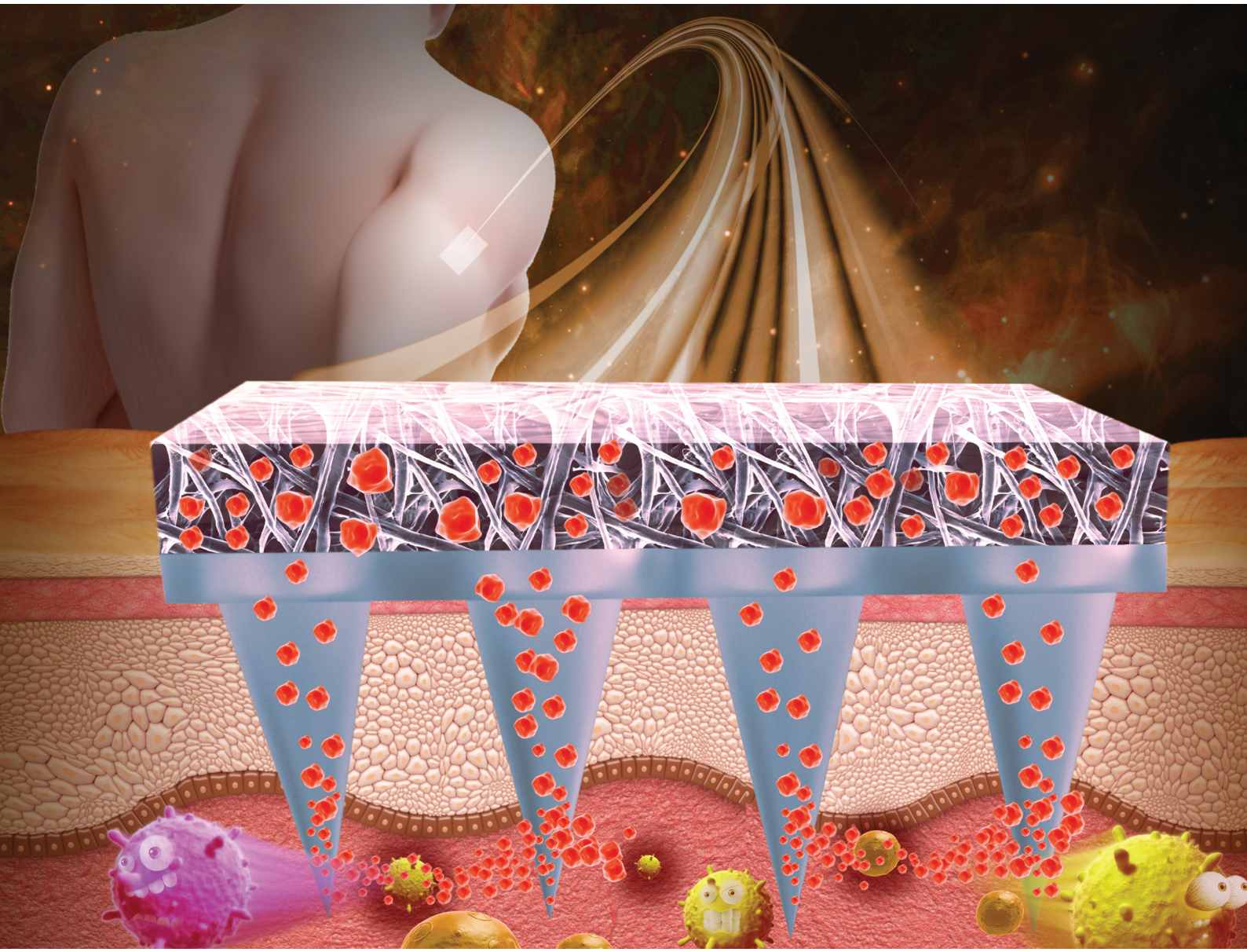

ISSN 2050-750X

ROYAL SOCIETY OF CHEMISTRY

PAPER

Ryan F. Donnelly *et al.*

Novel SmartReservoirs for hydrogel-forming microneedles to improve the transdermal delivery of rifampicin

Journal of Materials Chemistry B

ROYAL SOCIETY OF CHEMISTRY

PAPER

View Article Online
View Journal | View Issue

Cite this: J. Mater. Chem. B, 2024, 12, 4375

Novel SmartReservoirs for hydrogel-forming microneedles to improve the transdermal delivery of rifampicin

Abraham M. Abraham, Qonita Kurnia Anjani, Masoud Adhami, Aaron R. J. Hutton, Eneko Larrañeta and Ryan F. Donnelly *

Hydrogel-forming microneedles (HF-MNs) are composed of unique cross-linked polymers that are devoid of the active pharmaceutical ingredient (API) within the microneedle array. Instead, the API is housed in a reservoir affixed on the top of the baseplate of the HF-MNs. To date, various types of drug-reservoirs and multiple solubility-enhancing approaches have been employed to deliver hydrophobic molecules combined with HF-MNs. These strategies are not without drawbacks, as they require multiple manufacturing steps, from solubility enhancement to reservoir production. However, this current study challenges this trend and focuses on the delivery of the hydrophobic antibiotic rifampicin using SmartFilm-technology as a solubility-enhancing strategy. In contrast to previous techniques, smart drug-reservoirs (SmartReservoirs) for hydrophobic compounds can be manufactured using a one step process. In this study, HF-MNs and three different concentrations of rifampicin SmartFilms (SFs) were produced. Following this, both HF-MNs and SFs were fully characterised regarding their physicochemical and mechanical properties, morphology, Raman surface mapping, the interaction with the cellulose matrix and maintenance of the loaded drug in the amorphous form. In addition, their drug loading and transdermal permeation efficacy were studied. The resulting SFs showed that the API was intact inside the cellulose matrix within the SFs, with the majority of the drug in the amorphous state. SFs alone demonstrated no transdermal penetration and less than 20 ± 4 μg of rifampicin deposited in the skin layers. In contrast, the transdermal permeation profile using SFs combined with HF-MNs (*i.e.* SmartReservoirs) demonstrated a 4-fold increase in rifampicin deposition (80 ± 7 μg) in the skin layers and a permeation of approx. 500 ± 22 μg. Results therefore illustrate that SFs can be viewed as novel drug-reservoirs (*i.e.* SmartReservoirs) for HF-MNs, achieving highly efficient loading and diffusion properties through the hydrogel matrix.

Received 16th January 2024,
Accepted 7th March 2024

DOI: 10.1039/d4tb00110a

rsc.li/materials-b

1. Introduction

The human skin, considered to be the largest organ of the human body,[1,2] serves as the first line of defence against various pathogens and environmental factors.[3–7] Despite its protective role, disruption to the skin can result in exposure to infectious microorganisms.[3,8] This can give rise to infections within the superficial layers of the skin as well as in deep soft skin tissues.[7,9,10] In some instances this can be fatal, as seen in Methicillin-Resistant *S. aureus* (MRSA) infections.[11,12] A commonly used strategy to treat superficial skin infections involves the topical application of different antibiotics.[13,14] Nevertheless, the efficacy of topically applied antibiotics in treating systemic and deep soft tissue infections is often limited due to insufficient local drug concentrations.[15] While oral antibiotic treatment is usually prescribed, it is not without drawbacks.[16–18] Challenges can arise from drug stability in the gastrointestinal tract (GIT), along with the disruption of the GIT microbiome which could result in antimicrobial resistance.[18–20] Various strategies have been explored to target deep skin tissue and systemic infections whilst reducing potential side effects. These approaches have included the use of different nanocarriers, such as extracellular vesicles, liposomes, ethosomes, lipid and polymer nanoparticles within topical formulations.[21–27] These mentioned nanocarriers still pose numerous challenges which relate to time-consuming manufacturing or isolation processes.[23,28] Also, their effectiveness could be severely limited due to low encapsulation efficiency resulting in insufficient dosing.[28,29] In addition, these formulations typically require intravenous (IV) administration,

School of Pharmacy, Queen's University Belfast, Medical Biology Centre, 97 Lisburn Road, Belfast BT9 7BL, UK. E-mail: abraham.abraham@qub.ac.uk, r.donnelly@qub.ac.uk; Tel: +44 (0)2890 972 251

leading to whole body dosing, which can result in unnecessary side effects and drug-drug interactions. This route of antibiotic delivery is particularly challenging in developing countries due to limited access to trained medical professionals and the lack of provisions for safe needle disposal. Alternative formulation techniques offer a solution to the limited encapsulation efficiency, such as nanocrystals that are composed of 100% drug, which have been extensively investigated for their transdermal drug delivery properties.[30–34] However, literature reports have indicated that not all of these nanocarriers can successfully penetrate through intact skin and are therefore unable to target deep tissue infections or achieve therapeutic concentrations within the systemic circulation when applied topically or *via* a transdermal patch.[32,35,36]

A recent technology with high loading efficiency is SmartFilms® (SF), composed of cellulose based matrices that maintain the active pharmaceutical ingredient (API) in its amorphous form.[32,37–39] Previously, Eckert *et al.* modelled the delivery of curcumin, a hydrophobic drug molecule, using SF-technology.[32] They reported a significant improvement in the solubility of curcumin using SF, leading to the successful incorporation of the hydrophobic molecule in its amorphous form within the cellulose matrix.[32] Surprisingly, despite the improved biopharmaceutical properties of curcumin and the advantages offered by SF, the authors noted poor skin penetration efficacy in *in vitro* penetration studies using Franz diffusion cells.[32] This was attributed to curcumin being confined to the cellulose matrix of the SF, resulting in limited contact with the diffusion membrane.[32] In contrast, our current work overcomes the issue of poor wettability of SF. In this study, hydrogel-forming microneedles (HF-MNs), in combination with SF solubility-enhancing technology, have been used to deliver the hydrophobic antibiotic rifampicin across the skin layers. SFs resolve issues related to the properties of the API, by solubilising it in the amorphous form whilst achieving a high drug loading.[40] HF-MNs, as their name suggests, are micron-scale needles prepared by a crosslinking reaction from an aqueous mixture of different swellable polymers and supported by a baseplate.[18,41–45] HF-MNs are drug-free as the active ingredient is contained in a reservoir affixed on the top of the base of the HF-MNs. HF-MNs have the capacity to circumvent the outermost layer of the skin, known as the *stratum corneum*, without causing pain or lipohypertrophy as seen with repeated IV injections. Bypassing the *stratum corneum* allows for enhanced dissolution of rifampicin within the SF upon hydration with the skin's interstitial fluid. This occurs *in situ* through the transformation of HF-MNs into an aqueous hydrogel matrix. According to Fick's law, this leads to the diffusion of the drug contained within the SF into the skin layers, facilitating local deposition in the deep skin tissue or systemic absorption.[32,46–49] Based on this, increasing the loading efficiency of solubilized rifampicin within the SF is expected to deliver greater amounts of the lipophilic antibiotic across the skin. This will ultimately improve upon the permeation profiles observed in previous studies which have investigated the transdermal delivery of rifampicin using MNs.[43,50]

In this work, the aim was to demonstrate the potential of SF as an alternative novel smart drug reservoir for HF-MNs, presenting a simple platform to deliver poorly soluble drugs in their amorphous form. Rifampicin has been chosen to represent a difficult to deliver hydrophobic antibiotic[51,52] used for dermal infections.[50,53] Three different concentrations of rifampicin within the SFs were fabricated which served as drug reservoirs for HF-MNs. Following this, both HF-MNs and rifampicin-SFs were fully characterised regarding their physicochemical properties, morphology in addition to their drug loading and transdermal penetration efficacy. SFs were used as a bench control and their penetration profile was also directly compared with the SF-HF-MNs combination.

2. Materials and methods

2.1. Materials

Rifampicin was purchased from Alfa Aesar (Lancashire, UK). Methanol 96% (v/v), Poly(vinyl alcohol) with molecular weight of 85–124 kDa, citric acid, orthophosphoric acid, sodium lauryl sulphate and ascorbic acid were purchased from Sigma-Aldrich (Dorset, UK). Poly(vinyl pyrrolidone) K29-32 (PVP) with molecular weight of 58 kDa was provided by Ashland (Kidderminster, UK). Ultrapure water was obtained from a water purification system (HPLC grade, Elga PURELAB DV 25, Veolia Water Systems, Dublin, Ireland).

2.2. Methods

2.2.1. Preparation of rifampicin-SFs as drug reservoirs. Rifampicin-SFs were prepared as illustrated in (Fig. 1) according to the previously described protocol.[37] Briefly, tissue paper (Tork tissue rolls (54.5 m × 25 cm), Bedfordshire, UK) was used as the cellulose matrix and methanol was used as the solvent for rifampicin. The obtained alcoholic stock solution contained 20 mg mL^{-1} rifampicin. The paper was cut into small squares

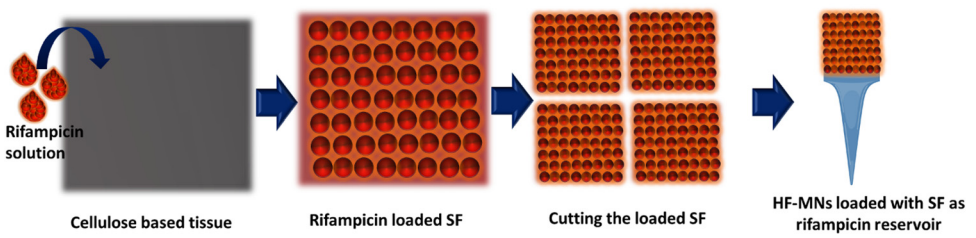

Fig. 1 Production of rifampicin-SFs (SmartFilms) as SmartReservoirs for the HF-MNs (hydrogel-forming MNs).

with a size of 10 cm × 10 cm (100 cm^2) and was loaded with 100 μL of the previously mentioned rifampicin solution onto the surface of the paper using a pipette. The matrix was left to dry at room temperature. The last two steps were repeated until approximately 100 mg rifampicin/100 cm^2 of the cellulose matrix (SF (1)) was loaded. Similar procedures were repeated to obtain an amount of 200 mg (SF (2)) and 500 mg (SF (3)) rifampicin/100 cm^2 per cellulose matrix. After drying, the obtained SFs (of the three concentrations) were cut into small pieces of 1 cm × 1 cm (1 cm^2) and were further characterized prior to skin permeation studies. The physical mixture was prepared by dry mixing the cellulose matrix and similar amounts of rifampicin.

2.2.2. Visualization of rifampicin-SFs as drug reservoirs. Rifampicin-SF reservoirs were visualised macroscopically and microscopically using a light microscope with an affixed colour camera (Leica Microsystems, Milton Keynes, Buckinghamshire, UK) and using scanning electron microscopy (SEM) with a Hitachi TM3030 tabletop SEM microscope (Chiyoda-ku, Tokyo, Japan). The SEM images were obtained without coating and under low vacuum and the energy used was adjusted on the dispersive X-ray analysis (EDX) mode with standard SEM carbon tape as the background. The loaded SFs were also compared with the pure drug, physical mixture and the unloaded SFs.

2.2.3. Determination of the crystallinity state using X-ray diffraction (X-RD) of rifampicin-SFs. X-RD analysis of pure rifampicin and the different loaded SFs was carried out using a MiniFlex II powder X-ray diffractometer with PDWL software (Rigaku Corporation, Tokyo, Japan). Patterns were collected in continuous mode in the angular range of 3–45° 2θ, with a step size of 0.01°, a scanning rate of 2° min^{-1}, a voltage of 30 kV, and a current of 15 mA.[32,43] The physical mixture and unloaded SF were used as controls.

2.2.4. Differential scanning calorimetry (DSC) of rifampicin-SFs. DSC analysis was performed on samples of pure rifampicin, the unloaded SF, physical mixture and the different loaded SFs using an Advantage Model Q100 DSC (TA Instruments, New Castle, DE). Samples of 3–10 mg were weighed accurately and placed in aluminium pans that were then sealed by crimping and subsequently heated at a rate of 10 °C per min from 30 to 250 °C under a nitrogen flow of 50 mL min^{-1}.[43,54]

2.2.5. Attenuated total reflection Fourier transform infrared (FTIR) of rifampicin-SFs. FTIR spectroscopy was used to analyse interactions present in pure rifampicin, unloaded SF, physical mixture and the three different loaded rifampicin-SFs using an Accutrac FT/IR-4100 Series (Jasco, Essex, U.K.) equipped with MIRacle diamond ATR accessory (Pike Technologies Ltd., Madison, WI). The IR spectra were scanned and recorded in the region ranging from 4000 to 600 cm^{-1} at room temperature. Resolution was maintained at 4.0 cm^{-1} throughout the analysis and the obtained spectra were the result of an average of 64 scans.[43,55]

2.2.6. Chemical analysis and drug content of rifampicin-SFs. Rifampicin content within the SFs was determined *via* high-performance liquid chromatography (HPLC) using a method described previously by Anjani *et al.*[43,55] Briefly, Agilent technologies 1220 infinity compacted LC series including a degasser, binary pump, auto injector and UV detector at 334 nm (Agilent Technologies UK Ltd, Stockport, UK) were used. A HPLC column (Phenomenex® Luna C18 (ODS1), 150 mm × 4.6 mm internal diameter, 5 μm packing) was obtained from Phenomenex (Cheshire, UK). The analysis was performed at room temperature, with an injection volume of 50 μL and a flow rate of 1 mL min^{-1}. The mobile phase was composed of 25 mM sodium dihydrogen phosphate buffer (with 1% v/v triethylamine (TEA), pH 6.8 adjusted using orthophosphoric acid) and methanol (30 : 70 v/v). The chromatograms were analysed using Agilent ChemStation® Software B.02.01. The International Council of Harmonisation (ICH) 2005 guidelines were followed as a reference to validate all the analytical methods.

2.2.7. Mechanical properties of rifampicin-SFs. The uniaxial tensile mechanical properties of rifampicin-SFs were tested and compared with a drug-free SF as well as with solvent only SF (as controls) using a TA.XTplus Texture Analyser (Stable Micro Systems, Surrey, UK) at a constant extension speed of 10.2 mm min^{-1}.[56,57] The SFs were cut to a dimension of 5 × 1 cm and the thickness of the SFs was measured using a calliper to calculate the cross-sectional area, and then clamped with a specific inter-clamp distance. The bottom and top ends of the 5 × 1 cm SFs were fixed in a horizontal position. Afterwards, the SFs were extended on the Texture Analyser using a controlled speed of 10.2 mm min^{-1}, until the SFs had completely ripped. The suture retention strength was calculated as load force (N)/(suture diameter (mm) SF thickness (mm)) as previously reported.[58] Force displacement figures were then recorded and the elastic modulus, offset yield strength, elongation at break were calculated from the obtained data. The offset yield strength of the tested SFs was obtained using the 0.2% offset method, as an approximation of the material's elastic limit.[59,60] Additionally, the elastic modulus was obtained as the slope of the initial linear region of the stress/strain plot as previously reported.[60,61] Moreover, elongation at break was obtained by generating the stress/strain plots of the analysed SFs.[61]

2.2.8. Raman mapping of rifampicin-SFs. TA RM5 Raman Microscope (Edinburgh Instruments, Edinburgh, UK) equipped with a 785 nm laser was used to characterise the SFs described in this work in a similar way reported previously.[62] Spectra were obtained using 20% laser power, a pinhole of 300 μm and a slit of 70 μm. A grid of 20 × 15 points was used to map the presence of rifampicin in the surface of the samples. A single Raman spectrum was obtained at each point using an exposure time of 1 s. The resulting spectra were processed with the Ramacle software (Edinburgh Instruments, Edinburgh, UK) by removing the background. The mapping was obtained by plotting the intensity of the peak at *ca.* 1340 cm^{-1}.

2.2.9. Preparation of the HF-MNs. A previously reported HF-MNs formulation was used in this study.[43,44] The HF-MNs formulation was cast from aqueous blends of 15% w/w Poly(vinyl alcohol), 10% w/w Poly(vinyl pyrrolidone), 1.5% w/w citric acid solutions (Table 1). These solutions were prepared

Table 1 Hydrogel formulation and the applied crosslinking conditions

Polymer name	Abbreviation	Molecular weight (kDa)	Percentage (%)
Poly(vinyl alcohol)	PVA	85–124	15
Poly(vinyl pyrrolidone) K29–32	PVP	58	10
Citric acid	CA	—	1.5
Water	—	—	q.s. 100
Crosslinking conditions			
Temperature (°C)	130		
Time (h)	3		

from stock solutions of 25% w/w PVA and 40% w/w PVP. The moulds were designed to obtain final patches of 121 needles with a height of ~600 μm. The microneedles were perpendicular to the base and of conical shape and arranged in an 11 × 11 formation. After drying of the casted HF-MNs at room temperature for 24 h, the polymers were thermally crosslinked at 130 °C for 3 h.

2.2.10. Height reduction and insertion profile of the HF-MNs. To test the resistance to compression of the HF-MNs, a TA.XTplus Texture Analyser (Stable Micro Systems, Surrey, UK) in compression mode was used following a previously reported method.[63] The HF-MNs were attached on the probe from the baseplate, with the needles facing the aluminium block. The TA was adjusted to a pre-test speed, test speed and post-test speed of 10, 0.5 and 10 mm s^{-1} respectively. The height of the microneedle arrays before and after testing was measured and recorded using a digital light microscope (Leica Microsystems, Milton Keynes, Buckinghamshire, UK). The percentage MN height reduction was then calculated using eqn (1):

$$\text{Needle height reduction } (\%) = \left(\frac{H_b - H_a}{H_b}\right) \times 100 \qquad (1)$$

where H_b is the height before compression and H_a is the height after compression.

Additionally, for the insertion efficiency of the obtained HF-MNs, a Texture Analyser and an artificial skin model composed of eight layers of Parafilm® M were used according to the protocol previously described by Larrañeta *et al.*[64] Insertion efficiency was calculated by eqn (2):

$$\text{Insertion efficiency in the Parafilm}^{®}\ (\%) = \left(\frac{\text{number of holes counted}}{\text{number of microneedles in an array}}\right) \times 100 \qquad (2)$$

Furthermore, the insertion characteristics of the MNs into the skin Parafilm® M model were examined using an EX-101 optical coherence tomography (OCT) microscope (Michelson Diagnostics Ltd, Kent, UK).[18,64] OCT images were captured to visualise the depth of needle insertion, and ImageJ® software (National Institutes of Health, Bethesda, MD, USA) was utilised to calculate the precise insertion depth.

2.2.11. *In vitro* permeation study of the SFs and the HF-MNs combined with the SFs as drug reservoirs. All samples prepared in this study were tested regarding their skin penetration/permeation profile as well as the amount of rifampicin deposited in the skin following the already published protocol.[43,50] Briefly, *in vitro* transdermal delivery of rifampicin from the formulated SFs combined with the HF-MNs was studied using the Franz cell apparatus and dermatomed (350 μm) neonatal porcine skin. For this, neonatal porcine skin was taken from stillborn piglets (less than 24 h after birth). Skin was shaved carefully using a razor followed by subjecting the skin to an electric dermatome (Integra Padgett® model B, Integra Life Sciences Corporation, Ratingen, Germany) to reach a thickness of 350 μm. The skin slices were then frozen at −20 °C until further use. The skin was pre-equilibrated in PBS (pH 7.4) for 30 min at room temperature before the skin penetration/permeation studies *in vitro*.

To achieve the sink conditions and prevent rifampicin degradation during the study, PBS (pH 7.4) composed of 1% w/v sodium lauryl sulphate and 1% w/v ascorbic acid was used as a release medium.[43] As it was likely that rifampicin would be deposited within the skin layers during the *in vitro* transdermal studies, it was essential to ensure the complete extraction of rifampicin from the skin. To do this, the skin surface area was wiped once with tissue soaked in PBS. Afterwards, skin samples of ~1 cm^2 were sectioned into small pieces using scissors and then placed into 2 mL Eppendorf tubes. Samples were subjected to a homogenization cycle in 500 μL ultrapure water using Tissue Lyser LT (Qiagen Ltd, Manchester, UK) at 50 Hz for 15 min. Following homogenization, 1000 μL of methanol was added to the same Eppendorf tubes. Once again, the homogenized skin in the aqueous-alcoholic mixture was homogenized again using the same above-mentioned manner. Ultimately, the samples were centrifuged at 15 000 rpm for 15 min, and the supernatant was collected to determine the extracted amount of rifampicin within the skin layers using the explained HPLC method (*cf.* 2.2.6.).

2.2.12. Statistical analysis. All experiments were performed in triplicate unless stated otherwise. GraphPad Prism 10 (GraphPad Software, San Diego, CA) was used for statistical analysis. Where appropriate, an unpaired *t*-test was used for comparison of two groups. Normal distribution of the data was analysed using the Shapiro–Wilk test. For the normally distributed data, a one-way analysis of variance (ANOVA) and post-hoc tests with Tukey correction were used for the comparison of multiple groups. In contrast, Kruskal–Wallis test was used for the non-parametric data. In all cases, data was reported as the mean ± standard deviation or the mean + standard deviation. *P*-Values < 0.05 were denoted as statistically significant.

3. Results and discussion

3.1. Characterization of the SFs

The production of rifampicin-SFs was successfully achieved, as illustrated in (Fig. 1) and visualised through both light microscopy and SEM. The macro and microscopic images showed a reddish-orange film of the API loaded SFs, progressively deepening in colour with increased rifampicin content. This clearly indicates an increased concentration of rifampicin within the cellulose matrix of the three SFs produced in this study (Fig. 2).

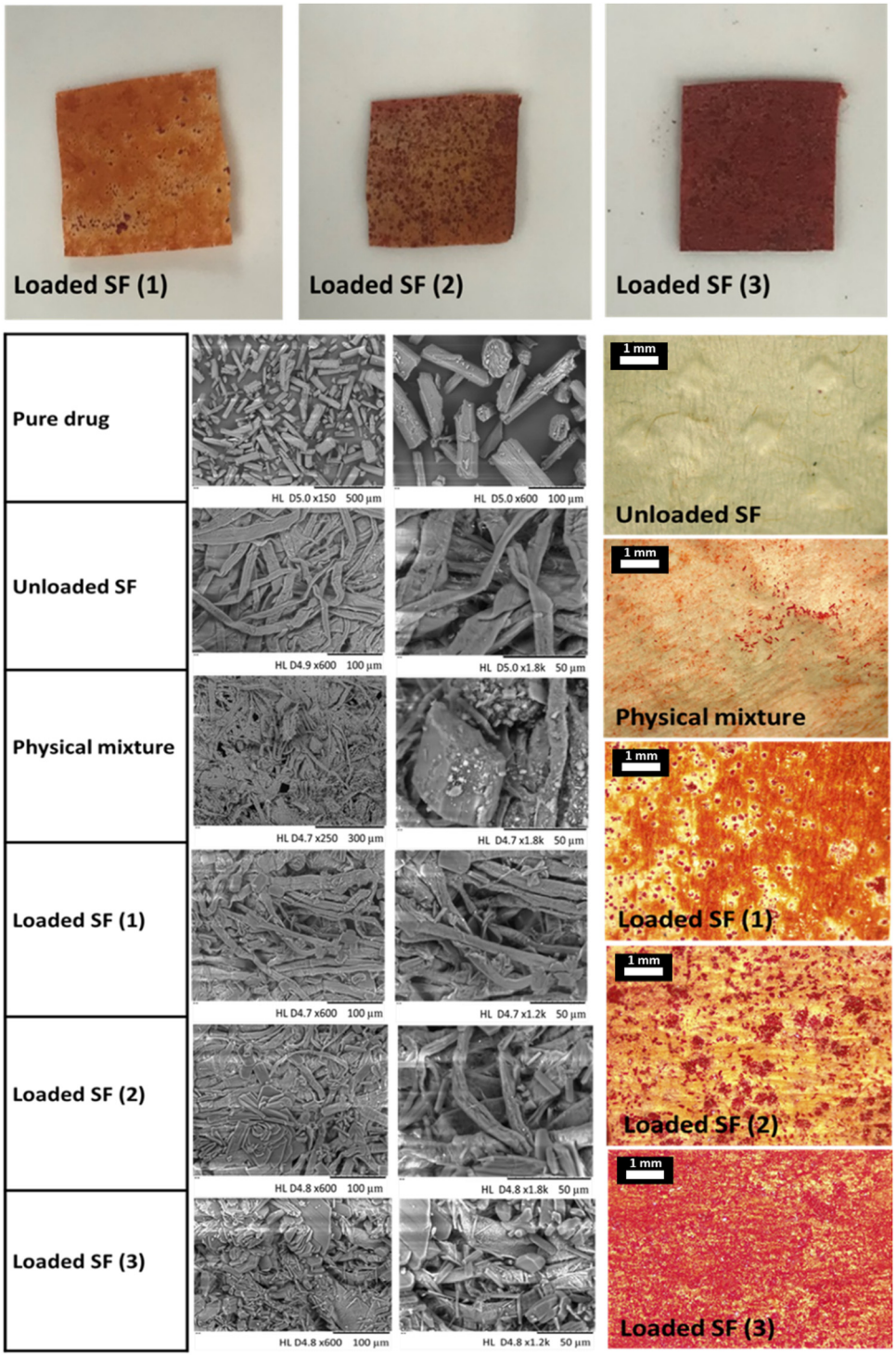

Fig. 2 Macroscopic, microscopic (using light microscope and SEM (showing the detailed structure of the cellulose-based matrix and their pores)) visualization of the obtained SFs (SmartFilms) in this study. Loaded SFs have been labelled according to drug loading, in which SF (1) represents the lowest rifampicin loading and SF (3) represents the highest rifampicin loading. Pure drug, unloaded SF and physical mixture were used as controls.

However, these two visualisation techniques lack the ability to view the drug incorporated inside the SF or the structure of the cellulose fibres used. To obtain a more detailed view, SEM was used, enabling the examination of the cellulose paper base's impact on the crystallization behaviour of the API. SEM images were obtained for the three different SFs loaded with rifampicin, and these were compared with the unloaded SF and the physical mixture. Analysis of the physical mixture revealed drug crystals adsorbed onto the surface of the SF, with no evidence of drug crystals within the cellulose network (Fig. 2). In contrast,

the addition of rifampicin solution showed that while a certain portion crystallized on the surface of all obtained SFs (*i.e.* the cellulose matrix), most of the rifampicin formed a distinct cobweb-like structure surrounded by the cellulose matrix (Fig. 2). SEM analysis indicated that the behaviour of the crystallization of rifampicin was influenced by the loading of different concentrations of the API (Fig. 2). This non-crystalline form, contrasting with pure rifampicin and the physical mixture, suggests the presence of amorphous drug particles within the cellulose matrix (*i.e.* located in the pores), aligning with previous studies performed by Abdelkader *et al.* and Stumpf.[37,40]

SF (1), which has the lowest drug loading, showed rifampicin in an amorphous form, but increasing the amount loaded (*i.e.* SF (2) and SF (3)) led to re-crystallization of the excess API outside of the cellulose matrix. This might be explained by referring to the proposed solubilization mechanism within SF which states that the cellulose fibres contained within the SF matrix hinder the crystallization of the loaded drug after solvent evaporation. This might be attributed to either the small pores (shown in SEM images in Fig. 2) that restrict crystal growth or the potential interactions within the SF matrix.[38,65,66] Hence, the quantity of drug loaded into the SFs is dependent on the number of pores, as an amount exceeding the pore capacity will result in re-crystallization of API on the cellulose fibres.[67] This was observed in the SEM images (Fig. 2) with loaded SF (3) showing full pores when compared to the unloaded SF.

Following SEM analysis, a more detailed investigation to further prove the amorphous state of rifampicin inside the SFs was performed using X-RD, DSC and FTIR (Fig. 3). X-RD analysis revealed several peaks at diffraction angles between 12.2° and 29.0° that indicate the crystalline form of pure rifampicin. Loading of rifampicin in the SFs resulted in diffractograms similar to the unloaded SF, which further explains the incorporation of the drug in the amorphous form in the cellulose fibre-based matrix and confirms that most of the drug was in the amorphous state. However, despite the SEM images of the physical mixture showing adsorbed drug crystals, only small peaks were noted in the X-RD diffractograms. To this end, it was necessary to employ additional methods to either prove or disprove the presence of API in the amorphous form within the cellulose matrix and to detect any possible reactions with the cellulose. For this, DSC, FTIR and Raman surface mapping were performed.

DSC analysis of the physical mixture resulted in two sharp peaks, similar to the peaks obtained for the unloaded SF and the pure rifampicin, indicating the presence of rifampicin in the crystalline form (Fig. 3). Additionally, the absence of a peak in the loaded SFs is attributed to the partial inclusion of rifampicin in the amorphous form inside the cellulose matrix. These DSC analysis findings are in line with the SEM images. In a similar fashion, FTIR analysis of the loaded SFs in comparison to the bench controls used (pure drug, unloaded SF and physical mixture) showed that the highlighted functional groups of pure drug were similar to those obtained in the spectra of loaded SFs (Fig. 3) and are similar to the data

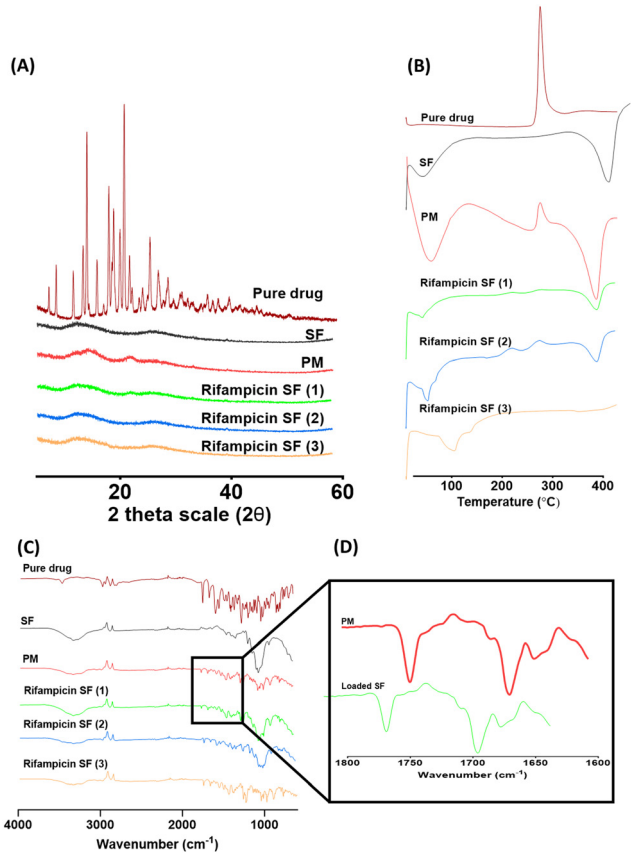

Fig. 3 Characterization of the crystallinity/amorphous state of rifampicin within the SFs (SmartFilms) and the controls (Pure drug, unloaded SF and physical mixture (PM)) in this study showing (A): X-RD diffractograms, (B): the DSC thermograms and (C): FTIR spectra. (D): FTIR spectra magnified associated with the specific groups to compare the physical mixture with the loaded representative SF.

reported in literature for rifampicin.[43] Interestingly, the bands associated to acetyl C=O (*ca.* 1725 cm^{-1}) and furanone C=O (*ca.* 1645 cm^{-1}) for rifampicin shifted to higher wavenumbers suggesting that these groups are involved in forming hydrogen bonds potentially with the cellulose matrix of the SFs.[68] This result confirmed no alterations of the drug molecule during its loading into the SFs. Rifampicin was found to reside within the cellulose matrix without any observed interactions or the formation of complexes with the cellulose matrix. This further indicates that the pores mechanism is the reason behind hindering the re-crystallization process upon solvent evaporation.

Raman was used to confirm drug distribution within the SFs (Fig. 4). Initially, Raman spectra was obtained for rifampicin (Fig. 4A). The more intense bands can be found between 1300 and 1400 cm^{-1} and have been attributed to the chromophore ring-stretching vibrations.[69] The same band can be found in the rifampicin rich domains of SF (1), SF (2) and SF (3) (Fig. 4A). The Raman spectra of blank films did not show any peaks (data not shown). The most intense peak in this region obtained at around 1340 cm^{-1} (highlighted with an arrow in Fig. 4A) was used to map the distribution of rifampicin in the SFs. Fig. 4B

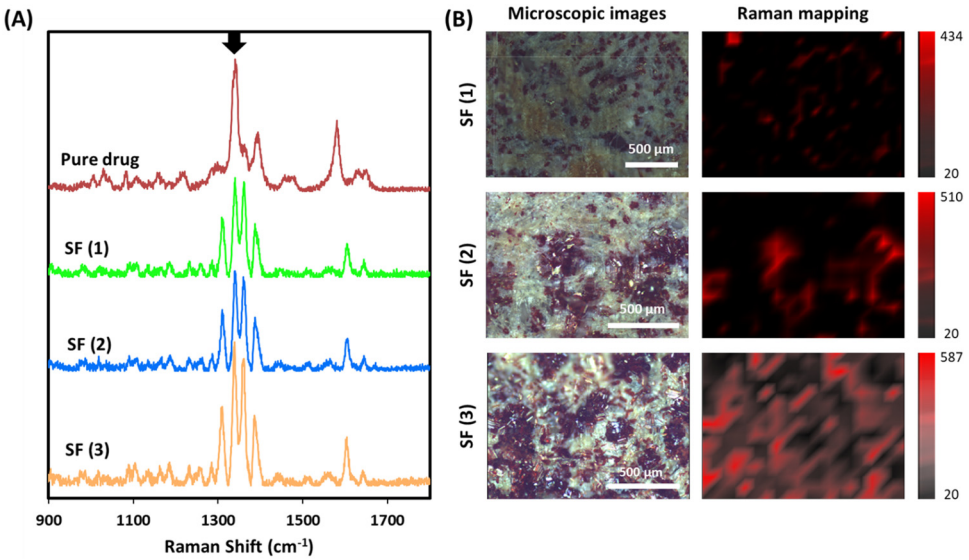

Fig. 4 (A) Raman spectra of pure rifampicin and Raman spectra obtained in rifampicin containing areas of SmartFilms (SF (1), SF (2) and SF (3)). The peak highlighted with an arrow was used for the mapping. (B) Microscopic images and the corresponding Raman surface mapping for SF (1), SF (2) and SF (3).

shows microscopic images of the SFs and the Raman mapping. SF (3) shows the highest amount of drug distributed through the surface of the film followed by SF (2). Finally, SF (1) presented the lowest amount of rifampicin. This is consistent with the results reported previously. Interestingly the intensity of some of the rifampicin peaks changed when the drug was loaded into SFs. This can be associated with the crystallinity change described before as the drug loaded into the SFs is amorphous. Noticeably, the intensity of the peak at around 1360 cm^{-1}, associated with C–OH vibrations, increases when rifampicin is loaded into SFs. Additionally, the intensity of the peak at around 1310 cm^{-1}, associated with vibrations of the ring, increases too when the drug is loaded into SF (1). These changes in vibrational modes recorded through Raman for rifampicin forming complexes has been reported previously for rifampicin adsorbed onto magnetite nanoparticles.[70] Additionally, changes in Raman peak intensity due to interactions with polymers and changes in crystallinity have been reported for other drugs.[71] These results suggest interactions between cellulose matrix within the SFs and the drug leading to drug amorphization. Therefore, these results are consistent with the results reported previously.

Furthermore, the mechanical properties of the SFs were studied. The mechanical properties were expressed by the elastic modulus, the offset yield strength, and the elongation at break of the SFs (Fig. 5). These properties describe the deformation of structural material under flexure. In this study, the effect of drug loading on the elastic modulus of the SFs was demonstrated. The loading of rifampicin into the cellulose matrix impacted the mechanical properties of the SFs. The elastic modulus of the SF containing the highest concentration of rifampicin (*i.e.*, SF (3)) decreased significantly ($p < 0.05$), equivalent to ~50%, in comparison to the unloaded SF and the SF treated with the solvent only (Fig. 5). In a similar fashion, the offset yield strength was also affected by increasing the drug content (Fig. 5). This could be attributed to two factors; the

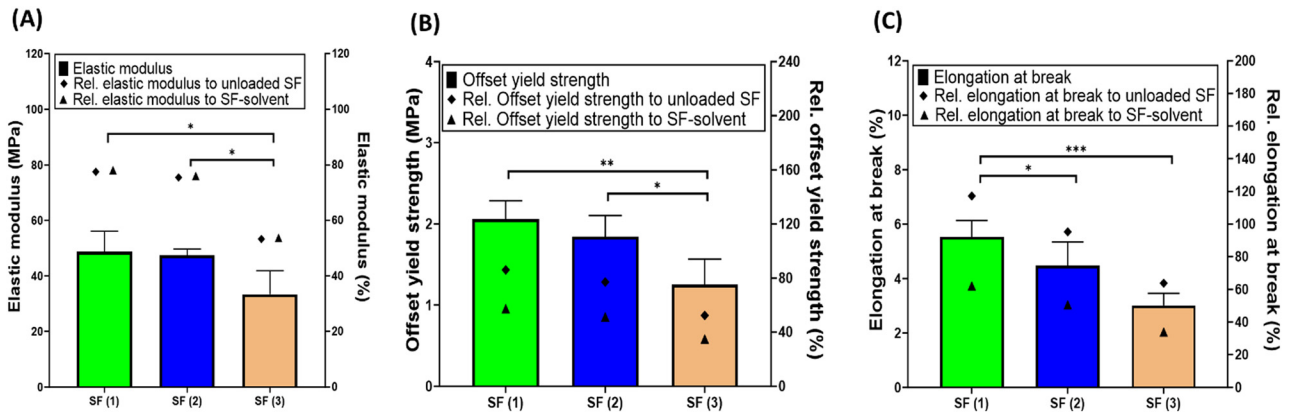

Fig. 5 Mechanical properties of the rifampicin-SFs (SmartFilms) in this study showing (A): the elastic modulus, (B): the offset yield strength and (C): the elongation at break. Unloaded SF and SF treated only with the used solvent only (without rifampicin) were used as bench controls (means + SD, $n = 5$).

higher filling (to the saturation level) of the pores in the cellulose matrix indicated by the SEM images (*cf.* Fig. 2) and/or the modification caused by the solvent.[67] In other words, the interaction of the cellulose within the SFs and the solvent results in skeletal contraction of these fibres (*cf.* Fig. 2) which indicates a possible change in the intramolecular hydrogen bonds of the cellulose matrix itself, leading to modification of the mechanical properties of the films. The skeletal contraction of these fibres reduces their width, thus increasing the pores size which in turn increases the concentration of amorphous drug within the pores. Specifically, filling the pores with amorphous drug led to greater expansion and elasticity.[67]

Nonetheless, the elongation at break of the SFs containing different rifampicin concentrations was lower than the values for the controls used (SF only and SF with solvent only) (Fig. 5C). This data is in a line with a study performed by Domínguez-Robles *et al.*[56,57,59]

Following the analysis of the mechanical properties, the rifampicin content within the SFs was analysed for the three concentrations of loaded SFs produced in this study. The data showed that all the SFs contain milligram amounts of rifampicin and the loading could be increased to $\sim$7 mg cm^{-2} (Fig. 6).

3.2. Characterization of the HF-MNs

The HF-MNs formulation chosen has been already investigated in detail regarding their properties by Anjani *et al.* and Tekko *et al.*[43,44] However, the mechanical characteristics mentioned in the previous studies were re-examined to ensure that the fabrication process in this study was in line with previously reported characteristics. The macroscopic, microscopic and SEM visualization of the obtained HF-MNs showed a homogeneous structure of the obtained microneedles with a sharp needle tip (Fig. 7A–F).

The mechanical strength characteristics of the manufactured HF-MNs were also analysed to ensure penetration through the *stratum corneum*.[72,73] The HF-MNs used in this study were tested

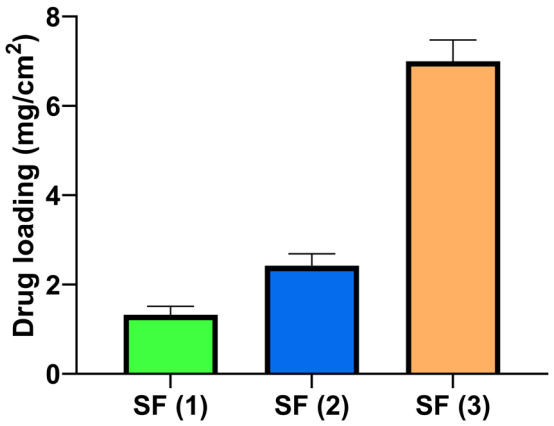

Fig. 6 The amount of rifampicin loaded within the three different SFs (SmartFilms) produced in this study expressed as mg cm^{-2} of each SF (means + SD, n = 3). The SFs represent the SmartReservoirs (SRs) when affixed on the top of the drug free HF-MNs (hydrogel-forming MNs) in this study.

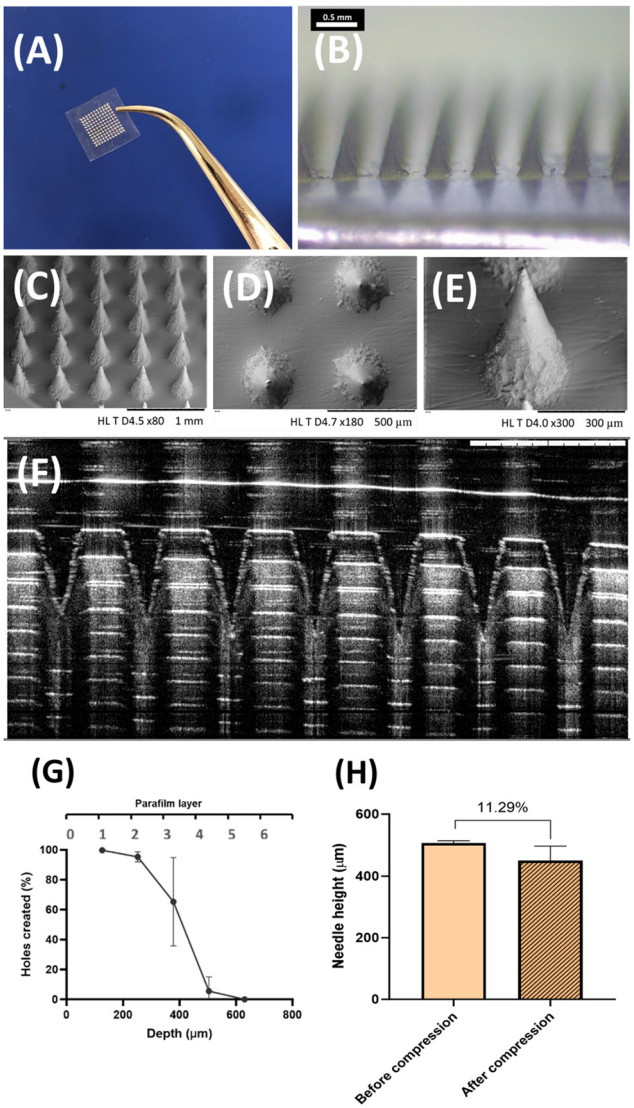

Fig. 7 Characterization of the obtained HF-MNs (hydrogel-forming MNs) in this study. (A): macroscopic image, (B): microscopic image (scale bar represents a length of 0.5 mm) and (C)–(E): SEM images. (F): OCT image of HF-MNs (the scale bar represents a length of 1 mm). (G): represents the percentage of holes created in each Parafilm®M layer and the insertion depth after insertion of HF-MNs produced in this study. (H): represents a comparison of the height reduction percentage of HF-MNs after the application of force of 32 N using TA. (means ± SD or means + SD, n = 3).

via insertion into eight layers of Parafilm®M. This is considered to be an accepted model to test the insertion profile of a MN. The MNs could penetrate the fourth layer of Parafilm® M (approx. 504 µm) (Fig. 7G). This indicates that more than 80% of the needle height could penetrate into the artificial membrane which is in agreement with data published previously.[43] Furthermore, percentage height reduction for the MN formulations was calculated following the application of an insertion force equal to average thumb pressure.[74] Fig. 7H shows that the reduction in the needle height was less than 12%, which is in line with the data reported previously and therefore shows good mechanical strength characteristics.[75] Based on the data obtained in this study, it could

be concluded that the manufactured HF-MNs align with previous work and are deemed appropriate for *in vitro* testing.

3.3. *In vitro* skin permeation study of rifampicin from SFs and HF-MNs

The transdermal permeation properties of rifampicin from SFs alone and combined with HF-MNs were examined over a 24 h period. The three different loaded SFs (SF (1), SF (2) and SF (3)) applied directly on the skin (*i.e.* in the absence of HF-MNs) showed no transdermal permeation after 24 h. These results are attributed to the dry film on the skin as illustrated in the macroscopic images taken after removing the loaded SFs from the skin (Fig. 8A). Furthermore, in these replicates, rifampicin-SFs demonstrated low drug deposition (less than 20 μg) in the upper skin layers (Fig. 9–11). This has proved that relying solely on SFs alone, *i.e.*, without the addition of HF-MNs, is insufficient in facilitating the transdermal permeation of the hydrophobic antibiotic. This data agrees with a study published by Eckert *et al.* that showed a very low skin penetration profile using the SF in the same *in vitro* model.[32] Consequently, using HF-MNs permits greater hydration of the SF which in turn results in improved transdermal permeation (more than 500 μg of rifampicin from SmartReservoir (3)) and/or dermal deposition (an amount between 60–80 μg of the API from the three

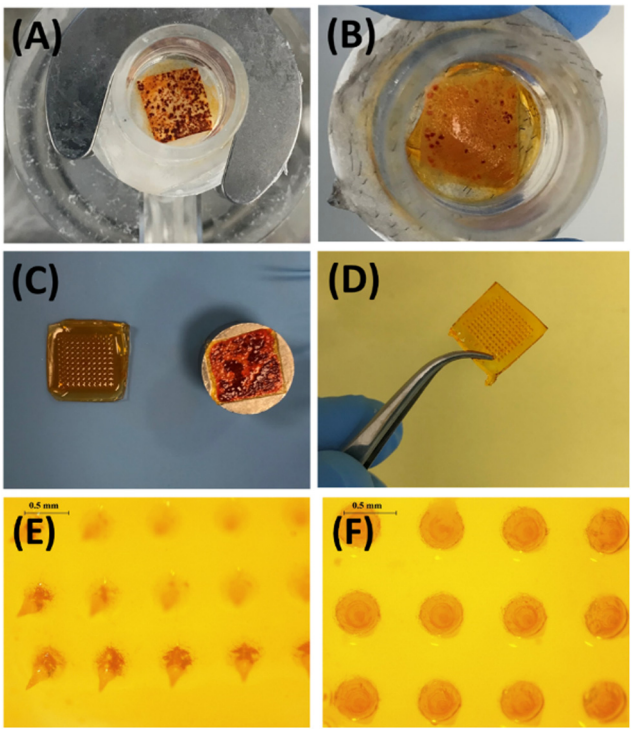

Fig. 8 Representative images of the SFs (SmartFilms) and the HF-MNs (hydrogel-forming MNs) after application on the skin and removing them after 24 h showing (A): dry SF (applied without HF-MNs), (B): wet SF (applied with the HF-MNs), (C) and (D): HF-MNs containing the drug (indicated by the colour of rifampicin) and the wet SF after removal, (E) and (F): light microscopic images of both sides of a representative HF-MNs showing the drug contained within the polymers after application (scale bar represents a length of 0.5 mm).

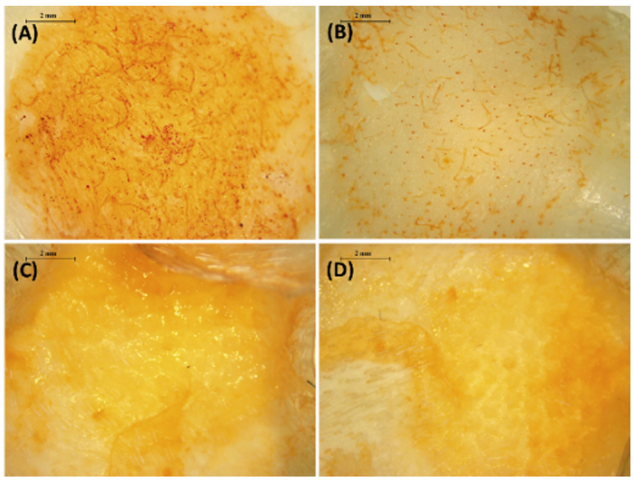

Fig. 9 Representative micrographs of the skin samples after the application of the SFs (SmartFilms) and the HF-MNs (hydrogel-forming MNs) after application on the skin and removing the formulations after 24 h. Upper panel: (A): SF without HF-MNs pre- cleaning, (B): SF without HF-MNs post-cleaning. Lower panel: (C): SF with HF-MNs pre- cleaning, (D): SF with HF-MNs post-cleaning. Scale bar represents a length of 2 mm.

concentrations of the SmartReservoirs (~6% of the released drug)) (Fig. 10). This hydration of the SmartReservoirs is shown in Fig. 8B and C, in which a hydrated SF in combination with a HF-MNs was visible following their removal 24 h post insertion. This is a result of the swelling that has occurred within the hydrogel network after insertion into the skin which enables passive diffusion of rifampicin from the SFs into the skin through the swollen HF-MNs (Fig. 8C–F). This can be explained according to Fick's law[31,46–48] as illustrated in eqn (3):

$$\frac{d_Q}{d_t} = \frac{D.V_k.A}{d}.C_v \quad (3)$$

where $\frac{d_Q}{d_t}$ is the amount of rifampicin penetrating from the SF into the HF-MNs, D the diffusion coefficient in the *stratum corneum*, V_k is the distribution coefficient between swollen hydrogel and the SF, A is the surface area of the application, d is the thickness of *stratum corneum* and the inserted length of the microneedles, C_v is the concentration of dissolved rifampicin within the swollen hydrogel (upon the release from the SmartReservoir).

Considering Fick's law, the increased solubility of rifampicin is a crucial factor to achieve improved skin penetration profile. This means increasing the kinetic solubility (C_v) using SF technology leads to a higher concentration gradient (d_Q/d_t) between the HF-MNs and the SFs of the solubilized rifampicin that led to an elevated passive diffusion of rifampicin from the SFs indicated by the linear permeation profile over 24 h (Fig. 11). To keep a high d_Q/d_t between the applied HF-MNs and the API loaded SF, a higher concentration was also investigated (*cf.* 3.1.), which resulted in a greater amount of the dissolved rifampicin upon the swelling of the HF-MNs leading to ~8–19% of the drug released and permeated/deposited in the skin (Fig. 10B and D). This demonstrates that the SF used as SmartReservoir in this study

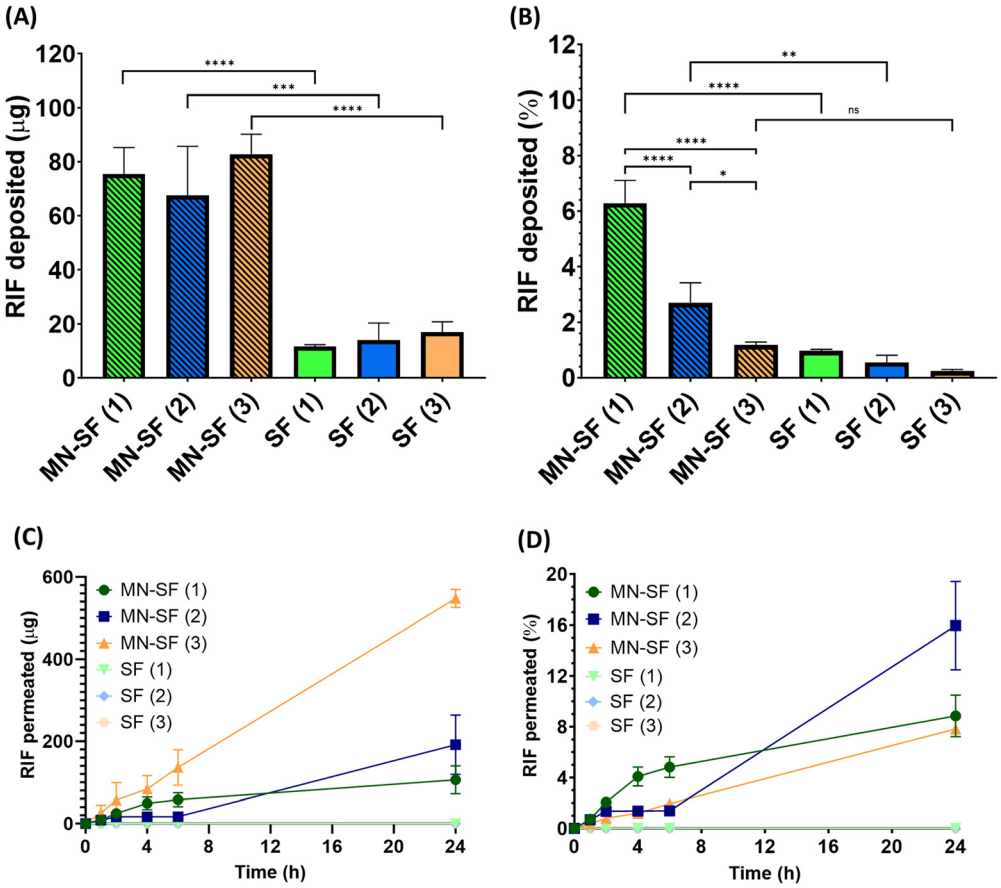

Fig. 10 Skin permeation profile showing the amount deposited and extracted from the skin after the application over 24 h of the SF (SmartFilm only without the HF-MNs (hydrogel-forming MNs) used as control) and MN-SF (SmartFilm with the HF-MNs (hydrogel-forming MNs)) obtained in this study (A): expressed in μg and (B): presented as cumulative percentage released from the SFs and deposited in the skin. (C): the amount permeated/penetrated expressed in μg and (D): cumulative percentage released from the SFs and permeated/penetrated into the skin and analysed after the permeation study *in vitro* over 24 h of the SF (SmartFilm only without the HF-MNs (hydrogel-forming MNs) used as control) and MN-SF (SmartFilm with the HF-MNs (hydrogel-forming MNs)) obtained in this study. (means ± SD or means + SD, n = 3).

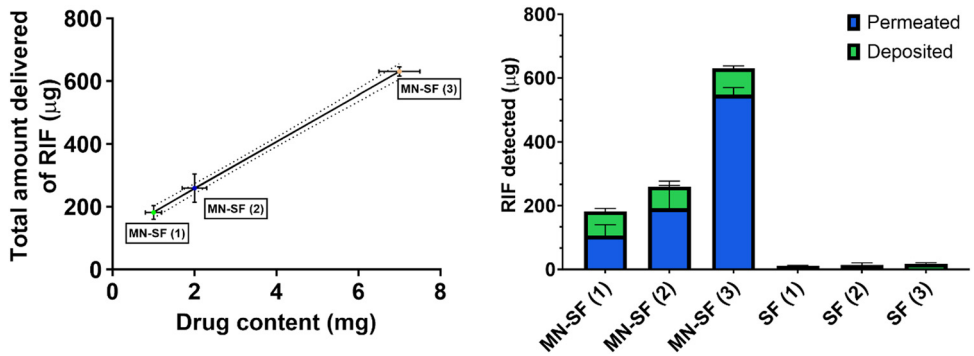

Fig. 11 The total amount of rifampicin delivered dermally (distributed within the skin layers) and transdermal (delivered to the blood stream) after the application over 24 h of the MN-SF (SmartFilm with the HF-MNs (hydrogel-forming MNs)) (left) obtained in this study. This shows a linear relation between rifampicin content and the total amount delivered. A comparison between the amount deposited *vs.* transdermal permeated of the total amount of rifampicin delivered (right). (means ± SD or means + SD, n = 3).

could sustain a high d_Q/d_t between the drug reservoir and the HF-MNs, ensuring a constant and prolonged diffusion of rifampicin from the SF into the swollen hydrogel. As a result, the API remains readily available for transdermal permeation.

After removing the formulation, the microscopic images of the skin showed a greater rifampicin deposition in the upper skin layers (indicated by the yellowish colour of the skin) for the SFs combined with the HF-MNs when compared to the SFs in

the absence of the HF-MNs (Fig. 9A–D). Furthermore, the extraction of rifampicin from the skin samples after 24 h application demonstrated a significant four-fold increase in rifampicin skin deposition when SFs were combined with HF-MNs compared to the SFs alone ($p < 0.05$) (Fig. 10A).

Ultimately, the *in vitro* transdermal permeation data obtained from the combination of the SF-HF-MNs further proved that the rifampicin released from the SFs into the skin through the hydrogel channel was continually increasing over the 24 h study time (Fig. 10B). According to the Korsmeyer–Peppas model, this permeation profile could be classified as a super case II transport.[32,63] In this model classification of the release kinetics is attributed to the swelling of the hydrogel in the first instance that results in swelling of the cellulose matrix. This is followed by a relaxation of the cellulose matrix upon the saturation of interstitial skin fluid that led to the swelling of the HF-MNs.[32] Thus, SF-HF-MNs obtained in this study demonstrated a higher deposition and permeation profile of rifampicin in the skin layers in comparison to the previous studies on the delivery of rifampicin using MNs.[43,50] Anjani *et al.* showed that ~0.10 mg of rifampicin was released from the lyophilised reservoirs used with HF-MNs after 24 h.[43] In another study, the authors delivered rifampicin using liposomes-loaded into dissolving MNs.[50] A total amount of less than 25 μg rifampicin could be delivered transdermally which could be attributed to the limited encapsulation efficiency of such nanocarriers and the limited amount of drug that can be loaded only in the tips of the dissolving MNs.[50] Therefore, the approach taken in our study (*i.e.* SF as smart drug reservoir for HF-MNs) offers a potential solution to overcome the challenges observed in these previous studies.[43,50]

To this end, Rifampicin-SFs were successfully produced and fully characterised regarding their mechanical, physicochemical properties and morphology. The data obtained confirmed that the drug was intact inside the cellulose matrix within the SFs. Despite the formation of crystals with increased drug loading, most of the rifampicin was in the amorphous state. Nevertheless, more studies are required to first understand the exact mechanism in which the drug is maintained in the amorphous state and secondly, to investigate the pores-based theory in greater detail. The transdermal permeation profile of the SFs applied directly on the skin resulted in no API within the Franz cell receiver compartment and only a small quantity of the hydrophobic antibiotic deposited in the skin layers. In contrast, the SFs combined with HF-MNs showed a well pronounced transdermal permeation and/or dermal deposition profile. Thus, the SmartReservoirs have shown potential in overcoming the challenges of the previous studies in delivering rifampicin using microneedles. The skin permeation of rifampicin achieved within this study showcases a 'smart' approach for the systemic and intradermal delivery of hydrophobic antibiotics. Ultimately, achieving a high skin permeation or dermal deposition of rifampicin using the new smart approach will be beneficial to tackle the challenges associated with topically applied formulations. In addition, unlike antibiotics delivered orally or by IV injection, HF-MNs can improve the systemic delivery of rifampicin for soft and deep skin tissue infections without causing pain and or issues associated with oral delivery such as the disruption to the GIT microbiome.

4. Conclusions

Novel SmartReservoirs made from paper have been reported and used for the first time as smart drug reservoirs for HF-MNs. This study has illustrated an efficient drug delivery system in which diffusion of a hydrophobic antibiotic from the SmartReservoirs into the swollen HF-MNs enables transdermal permeation across the skin. Thus, SFs can have their action in delivering a model hydrophobic drug across and into skin enhanced using HF-MNs. Ultimately, the new SmartReservoir-technology presented in this work is a simple technique that is easily scalable. Further studies are now needed to investigate the efficiency of the SmartReservoirs as a drug reservoir for HF-MNs with other drug molecules and using different hydrogel formulations. As our focus in this study was on enhancing the action of SFs, other studies comparing the SmartReservoirs to other drug reservoirs that have been used before with HF-MNs are now necessary. In addition, the antibacterial effect, the long-term application of the new smart system should be performed and combined with an *in vivo* study.

Author contributions

Abraham M Abraham: conceptualization, methodology, visualization, investigation, validation, data curation, writing – original draft. Qonita Kurnia Anjani: methodology, visualization, investigation, validation, data curation, writing – review & editing. Masoud Adhami: investigation & writing – review & editing. Aaron Hutton: writing – review & editing. Eneko Larrañeta: methodology, visualization, investigation, validation, data curation, writing – original draft, writing – review & editing, supervision. Ryan F. Donnelly: methodology, writing – review & editing, supervision.

Conflicts of interest

There are no conflicts to declare.

References

1 C. D'Amico, F. Fontana, N. El-Sayed, K. Elbadri, A. Correia, A. Rahikkala, J. Saarinen, M.-A. Shahbazi and H. A. Santos, Double-layered polyvinylpyrrolidone–poly(methyl vinyl ether- alt -maleic acid)-based microneedles to deliver meloxicam: an in vitro, in vivo, and short-term stability evaluation study, *Adv. Ther.*, 2023, **6**, 2300138, DOI: **10.1002/adtp.202300138**.

2 J. H. Lee, Y.-H. Hwang, M. Noh, J. H. Lee, J. B. Lee and H. Lee, Microencapsulation of alcohol solvents and high-content actives for efficient transdermal delivery, *Biomater. Sci.*, 2023, **11**, 7531–7540, DOI: **10.1039/d3bm01411h**.

3 A. L. Byrd, Y. Belkaid and J. A. Segre, The human skin microbiome, *Nat. Rev. Microbiol.*, 2018, **16**, 143–155, DOI: 10.1038/nrmicro.2017.157.
4 I. Peate, The skin: largest organ of the body, *Brit. J. Healthcare Assis.*, 2021, **15**, 446–451.
5 M. R. Prausnitz, P. M. Elias, T. J. Franz, M. Schmuth, J. C. Tsai, G. K. Menon, W. M. Holleran and K. R. Feingold, Skin barrier and transdermal drug delivery, *Dermatology*, 2012, **32**, 760–769.
6 W. Wang, K. Lu, C. Yu, Q. Huang and Y.-Z. Du, Nano-drug delivery systems in wound treatment and skin regeneration, *J. Nanobiotechnol.*, 2019, **17**, 82, DOI: 10.1186/s12951-019-0514-y.
7 E. A. Grice and J. A. Segre, The skin microbiome, *Nat. Rev. Microbiol.*, 2011, **9**, 244–253, DOI: 10.1038/nrmicro2537.
8 D. L. Stulberg, M. A. Penrod and R. A. Blatny, Common bacterial skin infections, *Am. Fam. Physician*, 2002, **66**, 119–124.
9 B. Dréno, E. Araviiskaia, E. Berardesca, G. Gontijo, M. Sanchez Viera, L. F. Xiang, R. Martin and T. Bieber, Microbiome in healthy skin, update for dermatologists, *J. Eur. Acad. Dermatol. Venereol.*, 2016, **30**, 2038–2047, DOI: 10.1111/jdv.13965.
10 P. L. J. M. Zeeuwen, J. Boekhorst, E. H. van den Bogaard, H. D. de Koning, P. M. C. van de Kerkhof, D. M. Saulnier, I. I. van Swam, S. A. F. T. van Hijum, M. Kleerebezem, J. Schalkwijk and H. M. Timmerman, Microbiome dynamics of human epidermis following skin barrier disruption, *Genome Biol.*, 2012, **13**, R101, DOI: 10.1186/gb-2012-13-11-r101.
11 M. Dryden, Complicated skin and soft tissue infections caused by methicillin-resistant Staphylococcus aureus: epidemiology, risk factors, and presentation, *Surg. Infect.*, 2008, **9**(1), s3–10, DOI: 10.1089/sur.2008.066.supp.
12 M. Pastagia, L. C. Kleinman, E. G. La Lacerda de Cruz and S. G. Jenkins, Predicting risk for death from MRSA bacteremia, *Emerging Infect. Dis.*, 2012, **18**, 1072–1080, DOI: 10.3201/eid1807.101371.
13 R. S. Mueller, K. Bergvall, E. Bensignor and R. Bond, A review of topical therapy for skin infections with bacteria and yeast, *Vet. Dermatol.*, 2012, **23**, 330–341, DOI: 10.1111/j.1365-3164.2012.01057.x.
14 C. Thornton Spann, S. C. Taylor and J. M. Weinberg, Topical antimicrobial agents in dermatology, *Clin. Dermatol.*, 2003, **21**, 70–77, DOI: 10.1016/s0738-081x(02)00320-6.
15 B. Godin, E. Touitou, E. Rubinstein, A. Athamna and M. Athamna, A new approach for treatment of deep skin infections by an ethosomal antibiotic preparation: an in vivo study, *J. Antimicrob. Chemother.*, 2005, **55**, 989–994, DOI: 10.1093/jac/dki125.
16 M. R. Prausnitz, Microneedles for transdermal drug delivery, *Adv. Drug Delivery Rev.*, 2004, **56**, 581–587, DOI: 10.1016/j.addr.2003.10.023.
17 Y.-Q. Yu, X. Yang, X.-F. Wu and Y.-B. Fan, Enhancing permeation of drug molecules across the skin via delivery in nanocarriers: novel strategies for effective transdermal applications, *Front. Bioeng. Biotechnol.*, 2021, **9**, 646554, DOI: 10.3389/fbioe.2021.646554.
18 P. E. McKenna, M. T. A. Abbate, L. K. Vora, A. H. Sabri, K. Peng, F. Volpe-Zanutto, I. A. Tekko, A. D. Permana, C. Maguire, D. Dineen, M.-C. Kearney, E. Larrañeta, A. J. Paredes and R. F. Donnelly, Polymeric microarray patches for enhanced transdermal delivery of the poorly soluble drug olanzapine, *ACS Appl. Mater. Interfaces*, 2023, **15**, 31300–31319, DOI: 10.1021/acsami.3c05553.
19 L. Brinkac, A. Voorhies, A. Gomez and K. E. Nelson, The threat of antimicrobial resistance on the human microbiome, *Microb. Ecol.*, 2017, **74**, 1001–1008, DOI: 10.1007/s00248-017-0985-z.
20 T. Nogueira, P. H. C. David and J. Pothier, Antibiotics as both friends and foes of the human gut microbiome: the microbial community approach, *Drug Dev. Res.*, 2019, **80**, 86–97, DOI: 10.1002/ddr.21466.
21 A. C. Apolinário, L. Hauschke, J. R. Nunes and L. B. Lopes, Towards nanoformulations for skin delivery of poorly soluble API: what does indeed matter?, *J. Drug Delivery Sci. Technol.*, 2020, **60**, 102045, DOI: 10.1016/j.jddst.2020.102045.
22 A. C. Apolinário, L. Hauschke, J. R. Nunes, F. R. Lourenço and L. B. Lopes, Design of multifunctional ethosomes for topical fenretinide delivery and breast cancer chemoprevention, *Colloids Surf., A*, 2021, **623**, 126745, DOI: 10.1016/j.colsurfa.2021.126745.
23 A. M. Abraham, S. Wiemann, G. Ambreen, J. Zhou, K. Engelhardt, J. Brüßler, U. Bakowsky, S.-M. Li, R. Mandic, G. Pocsfalvi and C. M. Keck, Cucumber-derived exosome-like vesicles and PlantCrystals for improved dermal drug delivery, *Pharmaceutics*, 2022, **14**, 476, DOI: 10.3390/pharmaceutics14030476.
24 K. Forier, K. Raemdonck, S. C. de Smedt, J. Demeester, T. Coenye and K. Braeckmans, Lipid and polymer nanoparticles for drug delivery to bacterial biofilms, *J. Controlled Release*, 2014, **190**, 607–623, DOI: 10.1016/j.jconrel.2014.03.055.
25 M. I. Mohammed, A. M. A. Makky, M. H. M. Teaima, M. M. Abdellatif, M. A. Hamzawy and M. A. F. Khalil, Transdermal delivery of vancomycin hydrochloride using combination of nano-ethosomes and iontophoresis: in vitro and in vivo study, *Drug Delivery*, 2016, **23**, 1558–1564, DOI: 10.3109/10717544.2015.1013200.
26 J. Marto, C. Vitor, A. Guerreiro, C. Severino, C. Eleutério, A. Ascenso and S. Simões, Ethosomes for enhanced skin delivery of griseofulvin, *Colloids Surf., B*, 2016, **146**, 616–623, DOI: 10.1016/j.colsurfb.2016.07.021.
27 X. Yang, G. Shi, J. Guo, C. Wang and Y. He, Exosome-encapsulated antibiotic against intracellular infections of methicillin-resistant Staphylococcus aureus, *Int. J. Nanomed.*, 2018, **13**, 8095–8104, DOI: 10.2147/IJN.S179380.
28 K. W. Witwer and J. Wolfram, Extracellular vesicles versus synthetic nanoparticles for drug delivery, *Nat. Rev. Mater.*, 2021, **6**, 103–106, DOI: 10.1038/s41578-020-00277-6.
29 H. Xiang, S. Xu, J. Li, Y. Li, X. Xue, Y. Liu, J. Li and X. Miao, Functional drug nanocrystals for cancer-target delivery,

J. Drug Delivery Sci. Technol., 2022, **76**, 103807, DOI: 10.1016/j.jddst.2022.103807.

30 M. B. McGuckin, J. Wang, R. Ghanma, N. Qin, S. D. Palma, R. F. Donnelly and A. J. Paredes, Nanocrystals as a master key to deliver hydrophobic drugs via multiple administration routes, *J. Controlled Release*, 2022, **345**, 334–353, DOI: 10.1016/j.jconrel.2022.03.012.

31 O. Pelikh, S. F. Hartmann, A. M. Abraham and C. M. Keck, in *Nanocrystals for Dermal Application*, ed. J. Cornier, Nanocosmetics, Springer International Publishing, Cham, (2019), pp. 161–177.

32 R. W. Eckert, S. Wiemann and C. M. Keck, Improved dermal and transdermal delivery of curcumin with SmartFilms and nanocrystals, *Molecules*, 2021, **26**, 1633, DOI: 10.3390/molecules26061633.

33 A. Fahr and X. Liu, Drug delivery strategies for poorly water-soluble drugs, *Expert Opin. Drug Delivery*, 2007, **4**, 403–416, DOI: 10.1517/17425247.4.4.403.

34 Y. Liu, J. Zhao, L. Wang, B. Yan, Y. Gu, P. Chang and Y. Wang, Nanocrystals technology for transdermal delivery of water-insoluble drugs, *Curr. Drug Delivery*, 2018, **15**, 1221–1229, DOI: 10.2174/1567201815666180518124345.

35 C. S. J. Campbell, L. R. Contreras-Rojas, M. B. Delgado-Charro and R. H. Guy, Objective assessment of nanoparticle disposition in mammalian skin after topical exposure, *J. Controlled Release*, 2012, **162**, 201–207, DOI: 10.1016/j.jconrel.2012.06.024.

36 P. Filipe, J. N. Silva, R. Silva, J. L. Cirne de Castro, M. Marques Gomes, L. C. Alves, R. Santus and T. Pinheiro, Stratum corneum is an effective barrier to TiO2 and ZnO nanoparticle percutaneous absorption, *Skin Pharmacol. Physiol.*, 2009, **22**, 266–275, DOI: 10.1159/000235554.

37 A. Abdelkader, E. Preis and C. M. Keck, SmartFilm tablets for improved oral delivery of poorly soluble drugs, *Pharmaceutics*, 2022, **14**, 1918, DOI: 10.3390/pharmaceutics14091918.

38 L. Heidrich, J. Ornik, R. Schesny, C. M. Keck, E. Castro-Camus and M. Koch, *Crystallinity investigation of poorly soluble drugs dispersed in paper using terahertz time-domain spectroscopy*, Optica Publishing Group, Washington, D.C., 2023.

39 Stefan Lemke, Ernst-Josef Strätling, Hans-Peter Welzel, Cornelia Margarete Keck DE102016000541A1, 2017.

40 F. Stumpf, Tabletten aus Papier – tablets made from paper – zur oralen Applikation schwerlöslicher Wirkstoffe, 2019.

41 R. F. Donnelly, T. R. R. Singh, M. J. Garland, K. Migalska, R. Majithiya, C. M. McCrudden, P. L. Kole, T. M. T. Mahmood, H. O. McCarthy and A. D. Woolfson, Hydrogel-forming microneedle arrays for enhanced transdermal drug delivery, *Adv. Funct. Mater.*, 2012, **22**, 4879–4890, DOI: 10.1002/adfm.201200864.

42 F. Volpe-Zanutto, L. K. Vora, I. A. Tekko, P. E. McKenna, A. D. Permana, A. H. Sabri, Q. K. Anjani, H. O. McCarthy, A. J. Paredes and R. F. Donnelly, Hydrogel-forming microarray patches with cyclodextrin drug reservoirs for long-acting delivery of poorly soluble cabotegravir sodium for HIV Pre-Exposure Prophylaxis, *J. Controlled Release*, 2022, **348**, 771–785, DOI: 10.1016/j.jconrel.2022.06.028.

43 Q. K. Anjani, A. D. Permana, Á. Cárcamo-Martínez, J. Domínguez-Robles, I. A. Tekko, E. Larrañeta, L. K. Vora, D. Ramadon and R. F. Donnelly, Versatility of hydrogel-forming microneedles in in vitro transdermal delivery of tuberculosis drugs, *Eur. J. Pharm. Biopharm.*, 2021, **158**, 294–312, DOI: 10.1016/j.ejpb.2020.12.003.

44 I. A. Tekko, G. Chen, J. Domínguez-Robles, R. R. S. Thakur, I. M. N. Hamdan, L. Vora, E. Larrañeta, J. C. McElnay, H. O. McCarthy, M. Rooney and R. F. Donnelly, Development and characterisation of novel poly (vinyl alcohol)/poly (vinyl pyrrolidone)-based hydrogel-forming microneedle arrays for enhanced and sustained transdermal delivery of methotrexate, *Int. J. Pharm.*, 2020, **586**, 119580, DOI: 10.1016/j.ijpharm.2020.119580.

45 Y. A. Naser, I. A. Tekko, L. K. Vora, K. Peng, Q. K. Anjani, B. Greer, C. Elliott, H. O. McCarthy and R. F. Donnelly, Hydrogel-forming microarray patches with solid dispersion reservoirs for transdermal long-acting microdepot delivery of a hydrophobic drug, *J. Controlled Release*, 2023, **356**, 416–433, DOI: 10.1016/j.jconrel.2023.03.003.

46 E. Chaiprateep, S. Wiemann, R. W. Eckert, C. S. Raab, S. Sengupta and C. M. Keck, Influence of dose, particle size & concentration on dermal penetration efficacy of curcumin, *Pharmaceutics*, 2023, **15**, 2645, DOI: 10.3390/pharmaceutics15112645.

47 N. Matharoo, H. Mohd and B. Michniak-Kohn, Transferosomes as a transdermal drug delivery system: Dermal kinetics and recent developments, *Wiley Interdiscip. Rev.: Nanomed. Nanobiotechnol.*, 2023, e1918, DOI: 10.1002/wnan.1918.

48 A. L. Lima, I. P. Gross, L. L. de Sá-Barreto, T. Gratieri, G. M. Gelfuso and M. Cunha-Filho, Extrusion-based systems for topical and transdermal drug delivery, *Expert Opin. Drug Delivery*, 2023, **20**, 979–992, DOI: 10.1080/17425247.2023.2241362.

49 J. He, Y. Zhang, X. Yu and C. Xu, Wearable patches for transdermal drug delivery, *Acta Pharm. Sin. B*, 2023, **13**, 2298–2309, DOI: 10.1016/j.apsb.2023.05.009.

50 Q. K. Anjani, A. K. Pandya, S. Demartis, J. Domínguez-Robles, N. Moreno-Castellanos, H. Li, E. Gavini, V. B. Patravale and R. F. Donnelly, Liposome-loaded polymeric microneedles for enhanced skin deposition of rifampicin, *Int. J. Pharm.*, 2023, **646**, 123446, DOI: 10.1016/j.ijpharm.2023.123446.

51 K. J. C. Melo, M. A. B. Henostroza, R. Löbenberg and N. A. Bou-Chacra, Rifampicin nanocrystals: towards an innovative approach to treat tuberculosis, *Mater. Sci. Eng., C*, 2020, **112**, 110895, DOI: 10.1016/j.msec.2020.110895.

52 A. Viçosa, J.-J. Letourneau, F. Espitalier and M. Inês Ré, An innovative antisolvent precipitation process as a promising technique to prepare ultrafine rifampicin particles, *J. Cryst. Growth*, 2012, **342**, 80–87, DOI: 10.1016/j.jcrysgro.2011.09.012.

53 N. K. Tsankov and J. A. Kamarashev, Rifampin in dermatology, *Int. J. Dermatol.*, 1993, **32**, 401–406, DOI: 10.1111/j.1365-4362.1993.tb02807.x.

54 N. K. Martin, J. Domínguez-Robles, S. A. Stewart, V. A. Cornelius, Q. K. Anjani, E. Utomo, I. García-Romero, R. F. Donnelly, A. Margariti, D. A. Lamprou and E. Larrañeta, Fused deposition modelling for the development of drug loaded

cardiovascular prosthesis, *Int. J. Pharm.*, 2021, **595**, 120243, DOI: 10.1016/j.ijpharm.2021.120243.

55 Q. K. Anjani, J. Domínguez-Robles, E. Utomo, M. Font, M. C. Martínez-Ohárriz, A. D. Permana, Á. Cárcamo-Martínez, E. Larrañeta and R. F. Donnelly, Inclusion complexes of rifampicin with native and derivatized cyclodextrins: in silico modeling, formulation, and characterization, *Pharmaceuticals*, 2021, **15**, 20, DOI: 10.3390/ph15010020.

56 J. Domínguez-Robles, E. Utomo, V. A. Cornelius, Q. K. Anjani, A. Korelidou, Z. Gonzalez, R. F. Donnelly, A. Margariti, M. Delgado-Aguilar, Q. Tarrés and E. Larrañeta, TPU-based antiplatelet cardiovascular prostheses prepared using fused deposition modelling, *Mater. Des.*, 2022, **220**, 110837, DOI: 10.1016/j.matdes.2022.110837.

57 J. Domínguez-Robles, T. Shen, V. A. Cornelius, F. Corduas, E. Mancuso, R. F. Donnelly, A. Margariti, D. A. Lamprou and E. Larrañeta, Development of drug loaded cardiovascular prosthesis for thrombosis prevention using 3D printing, *Mater. Sci. Eng., C*, 2021, **129**, 112375, DOI: 10.1016/j.msec.2021.112375.

58 P. Punnakitikashem, D. Truong, J. U. Menon, K. T. Nguyen and Y. Hong, Electrospun biodegradable elastic polyurethane scaffolds with dipyridamole release for small diameter vascular grafts, *Acta Biomater.*, 2014, **10**, 4618–4628, DOI: 10.1016/j.actbio.2014.07.031.

59 J. Domínguez-Robles, C. Mancinelli, E. Mancuso, I. García-Romero, B. F. Gilmore, L. Casettari, E. Larrañeta and D. A. Lamprou, 3D printing of drug-loaded thermoplastic polyurethane meshes: a potential material for soft tissue reinforcement in vaginal surgery, *Pharmaceutics*, 2020, **12**, 63, DOI: 10.3390/pharmaceutics12010063.

60 J. S. Afonso, P. A. L. S. Martins, M. J. B. C. Girao, R. M. Natal Jorge, A. J. M. Ferreira, T. Mascarenhas, A. A. Fernandes, J. Bernardes, E. C. Baracat, G. Rodrigues de Lima and B. Patricio, Mechanical properties of polypropylene mesh used in pelvic floor repair, *Int. Urogynecol. J.*, 2008, **19**, 375–380, DOI: 10.1007/s00192-007-0446-1.

61 K. A. McKenna, M. T. Hinds, R. C. Sarao, P.-C. Wu, C. L. Maslen, R. W. Glanville, D. Babcock and K. W. Gregory, Mechanical property characterization of electrospun recombinant human tropoelastin for vascular graft biomaterials, *Acta Biomater.*, 2012, **8**, 225–233, DOI: 10.1016/j.actbio.2011.08.001.

62 C. Zhang, S. A. Jahan, J. Zhang, M. B. Bianchi, F. Volpe-Zanutto, S. M. Baviskar, A. Rodriguez-Abetxuko, D. Mishra, E. Magee, B. F. Gilmore, T. R. R. Singh, R. F. Donnelly, E. Larrañeta and A. J. Paredes, Curcumin nanocrystals-in-nanofibres as a promising platform for the management of periodontal disease, *Int. J. Pharm.*, 2023, **648**, 123585, DOI: 10.1016/j.ijpharm.2023.123585.

63 K. Peng, L. K. Vora, J. Domínguez-Robles, Y. A. Naser, M. Li, E. Larrañeta and R. F. Donnelly, Hydrogel-forming microneedles for rapid and efficient skin deposition of controlled release tip-implants, *Mater. Sci. Eng., C*, 2021, **127**, 112226, DOI: 10.1016/j.msec.2021.112226.

64 E. Larrañeta, J. Moore, E. M. Vicente-Pérez, P. González-Vázquez, R. Lutton, A. D. Woolfson and R. F. Donnelly, A proposed model membrane and test method for microneedle insertion studies, *Int. J. Pharm.*, 2014, **472**, 65–73, DOI: 10.1016/j.ijpharm.2014.05.042.

65 L. Heidrich, A. Abdelkader, J. Ornik, E. Castro-Camus, C. M. Keck and M. Koch, Terahertz spectroscopy for non-destructive solid-state investigation of norfloxacin in paper tablets after wet granulation, *Pharmaceutics*, 2023, **15**, 1786, DOI: 10.3390/pharmaceutics15071786.

66 J. Ornik, L. Heidrich, R. Schesny, E. Castro-Camus, C. M. Keck and M. Koch, Non-destructive crystallinity assessment of indomethacin in tablets made from smartFilms® using terahertz time-domain spectroscopy, *Sci. Rep.*, 2022, **12**, 6099, DOI: 10.1038/s41598-022-10041-1.

67 Jan Ornik, Terahertz Time-Domain Spectroscopy of Poorly Soluble Pharmaceuticals, Germany, 2023.

68 S. Agrawal, Y. Ashokraj, P. V. Bharatam, O. Pillai and R. Panchagnula, Solid-state characterization of rifampicin samples and its biopharmaceutic relevance, *Eur. J. Pharm. Sci.*, 2004, **22**, 127–144, DOI: 10.1016/j.ejps.2004.02.011.

69 B. D. Howes, L. Guerrini, S. Sanchez-Cortes, M. P. Marzocchi, J. V. Garcia-Ramos and G. Smulevich, The influence of pH and anions on the adsorption mechanism of rifampicin on silver colloids, *J. Raman Spectrosc.*, 2007, **38**, 859–864, DOI: 10.1002/jrs.1727.

70 Q. S. Ferreira, S. W. Da Silva, C. M. B. Santos, G. C. Ribeiro, L. R. Guilherme and P. C. Morais, Rifampicin adsorbed onto magnetite nanoparticle: SERS study and insight on the molecular arrangement and light effect, *J. Raman Spectrosc.*, 2015, **46**, 765–771, DOI: 10.1002/jrs.4718.

71 H. Ueda, Y. Ida, K. Kadota and Y. Tozuka, Raman mapping for kinetic analysis of crystallization of amorphous drug based on distributional images, *Int. J. Pharm.*, 2014, **462**, 115–122, DOI: 10.1016/j.ijpharm.2013.12.025.

72 P. Makvandi, M. Kirkby, A. R. J. Hutton, M. Shabani, C. K. Y. Yiu, Z. Baghbantaraghdari, R. Jamaledin, M. Carlotti, B. Mazzolai, V. Mattoli and R. F. Donnelly, Engineering microneedle patches for improved penetration: analysis, skin models and factors affecting needle insertion, *Nano-Micro Lett.*, 2021, **13**, 93, DOI: 10.1007/s40820-021-00611-9.

73 A. J. Paredes, A. D. Permana, F. Volpe-Zanutto, M. N. Amir, L. K. Vora, I. A. Tekko, N. Akhavein, A. D. Weber, E. Larrañeta and R. F. Donnelly, Ring inserts as a useful strategy to prepare tip-loaded microneedles for long-acting drug delivery with application in HIV pre-exposure prophylaxis, *Mater. Des.*, 2022, **224**, 111416, DOI: 10.1016/j.matdes.2022.111416.

74 A. H. B. Sabri, Q. K. Anjani and R. F. Donnelly, Synthesis and characterization of sorbitol laced hydrogel-forming microneedles for therapeutic drug monitoring, *Int. J. Pharm.*, 2021, **607**, 121049, DOI: 10.1016/j.ijpharm.2021.121049.

75 R. F. Donnelly, R. Majithiya, T. R. R. Singh, D. I. J. Morrow, M. J. Garland, Y. K. Demir, K. Migalska, E. Ryan, D. Gillen, C. J. Scott and A. D. Woolfson, Design, optimization and characterisation of polymeric microneedle arrays prepared by a novel laser-based micromoulding technique, *Pharm. Res.*, 2011, **28**, 41–57, DOI: 10.1007/s11095-010-0169-8.

